Assessing the Impact of the Covariance Localization Radius when Assimilating Infrared Brightness Temperature Observations Using an Ensemble Kalman Filter

JASON A. OTKIN

Cooperative Institute for Meteorological Satellite Studies, University of Wisconsin—Madison, Madison, Wisconsin

ABSTRACT

A regional-scale Observing System Simulation Experiment is used to examine how changes in the horizontal covariance localization radius employed during the assimilation of infrared brightness temperature observations in an ensemble Kalman filter assimilation system impacts the accuracy of atmospheric analyses and short-range model forecasts. The case study tracks the evolution of several extratropical weather systems that occurred across the contiguous United States during 7–8 January 2008. Overall, the results indicate that assimilating 8.5-μm brightness temperatures improves the cloud analysis and forecast accuracy, but has the tendency to degrade the water vapor mixing ratio and thermodynamic fields unless a small localization radius is used. Vertical cross sections showed that varying the localization radius had a minimal impact on the shape of the analysis increments; however, their magnitude consistently increased with increasing localization radius. By the end of the assimilation period, the moisture, temperature, cloud, and wind errors generally decreased with decreasing localization radius and became similar to the Control case in which only conventional observations were assimilated if the shortest localization radius was used. Short-range ensemble forecasts showed that the large positive impact of the infrared observations on the final cloud analysis diminished rapidly during the forecast period, which indicates that it is difficult to maintain beneficial changes to the cloud analysis if the moisture and thermodynamic forcing controlling the cloud evolution are not simultaneously improved. These results show that although assimilation of infrared observations consistently improves the cloud field regardless of the length of the localization radius, it may be necessary to use a smaller radius to also improve the accuracy of the moisture and thermodynamic fields.

1. Introduction

Ensemble Kalman filter (EnKF) data assimilation systems (Evensen 1994) use a Monte Carlo approach to estimate the prior or background error covariance matrix that in combination with the assumed observation error is used to spread information from an observation spatially and between observed and unobserved variables. The ensemble size is typically several orders of magnitude smaller than the dimension of the model state vector; therefore, the covariance matrix tends to be severely rank deficient. This limits the ability of the assimilation system to modify the analysis in areas not sampled by the ensemble subspace and can lead to degraded analyses because of the presence of spurious correlations (Hacker et al. 2007). A common method used to mitigate the negative impact of spurious correlations

and also increase the rank of the ensemble is to localize the covariance matrix around each observation. The primary goal of localization is to disregard potentially spurious correlations that occur far from an observation, while preserving the larger and more meaningful correlations closer to the observation (Houtekamer and Mitchell 1998). Spatial covariance localization is based on the assumption that correlations generally decrease with increasing separation distance away from an observation (e.g., Hollingsworth and Lönnberg 1986) and that the analysis can be improved if the localization radius is large enough to encompass most of the relevant correlations between an observation and the model state, but small enough to eliminate spurious long-distance correlations (Yoon et al. 2010).

Early work by Houtekamer and Mitchell (1998, 2001) and Hamill et al. (2001) showed that a distance-based reduction of the background error covariance estimates improved assimilation performance. Covariances between an observation and the model state vector were reduced by performing an element-wise multiplication

Corresponding author address: Jason A. Otkin, 1225 W. Dayton St., Madison, WI 53706.
E-mail: jason.otkin@ssec.wisc.edu

of the background error covariance matrix calculated from the ensemble and a correlation function containing compact local support (e.g., Gaspari and Cohn 1999). Anderson (2007b) describes a hierarchical filter that is computationally expensive to use, but allows observations to effectively impact state variables even when the distance between the observation and the state variables is difficult to define (such as for satellite radiances). Hacker et al. (2007) have shown that both hierarchical filters and rational functions (such as Gaspari–Cohn) are able to effectively improve covariance estimates for small ensemble sizes when assimilating surface observations. Their results also indicate that the ability to specify different localization functions for different observation and state variable combinations is potentially useful. Bishop and Hodyss (2009a,b) have shown that using an adaptive methodology to generate localization functions that move with the true error correlation functions and adapt to the width of these functions leads to more accurate analyses than can be obtained using a static, nonvarying localization radius. Spectral localization of background error covariances has also been shown to systematically reduce model error (Buehner and Charron 2007).

To optimize assimilation performance, it is often necessary to conduct sensitivity tests to determine the optimal localization radius for each observation type since severe localization can cause substantial imbalances in the analysis that can accumulate with time and negatively impact model performance (Mitchell et al. 2002; Kepert 2009). Vertical covariance localization is difficult for satellite radiances since they are an integrated measure sensitive to a potentially broad layer of the atmosphere. For infrared radiances, the vertical level at which an observation has its greatest sensitivity (i.e., where the weighting function peaks) is typically a function of highly variable fields such as temperature, water vapor, clouds, and aerosols, which makes it difficult to localize radiances vertically in space using predefined functions. Localization in radiance space is a possible alternative; however, Campbell et al. (2010) have shown that it is generally better to localize radiances in model space since nonzero correlations between channels with broad, overlapping weighting functions can be incorrectly eliminated with radiance space localization.

Satellite radiances are the most numerous and widely available observations of the atmosphere and are a critical component of most global and regional assimilation systems. Advanced sensors on board existing (and future) satellite platforms provide accurate radiance measurements that provide important information about atmospheric moisture, temperature, wind, and clouds. Many prior studies have shown that assimilation of

infrared and microwave radiances and satellite-derived temperature and water vapor profile retrievals for clear-sky pixels has a large positive impact on forecast skill, especially where conventional observations are scarce (e.g., Tracton et al. 1980; Halem et al. 1982; Andersson et al. 1991; Mo et al. 1995; Derber and Wu 1998; McNally et al. 2000; Bouttier and Kelly 2001; Chevallier et al. 2004; McNally et al. 2006; Le Marshall et al. 2006; Xu et al. 2009; McCarty et al. 2009; Collard and McNally 2009). Several recent studies have also shown that assimilation of cloudy infrared observations in ensemble and variational assimilation systems improves the 3D cloud structure and forecast skill in cloud-resolving and global circulation models (Vukicevic et al. 2004, 2006; Reale et al. 2008; Otkin 2010; Stengel et al. 2010; Seaman et al. 2010). Encouraging results have also been obtained by extending the four-dimensional variational data assimilation (4DVAR) analysis control vector to include parameters such as cloud-top pressure and cloud fraction (McNally 2009).

In this study, results from a regional-scale Observing System Simulation Experiment (OSSE) will be used to evaluate how changes in the horizontal covariance localization radius used during the assimilation of clear and cloudy-sky infrared brightness temperatures (which will be used interchangeably with "radiances") impacts the accuracy of atmospheric analyses and short-term model forecasts. Simulated observations from the Advanced Baseline Imager (ABI) to be launched on board the Geostationary Operational Environmental Satellite (GOES)-R in 2016 will be employed. The ABI is a 16-band imager containing 2 visible, 4 near-infrared, and 10 infrared bands. Accurate radiance and reflectance measurements will provide detailed information about atmospheric water vapor, surface and cloud-top properties, sea surface temperature, and aerosol and trace gas components with high spatial and temporal resolution (Schmit et al. 2005). The paper is organized as follows. Section 2 contains a description of the data assimilation system and simulated observations with an overview of the case study provided in section 3. Results are shown in section 4 with conclusions presented in section 5.

2. Experimental design

a. Forecast model

Version 3.0.1.1 of the Weather Research and Forecasting (WRF) model was used for this study. WRF is a sophisticated numerical weather prediction model that solves the compressible nonhydrostatic Euler equations cast in flux form on a mass-based terrain-following vertical coordinate system. Prognostic variables include

the horizontal and vertical wind components, water vapor mixing ratio, various cloud microphysical fields, and the perturbation potential temperature, geopotential, and surface pressure of dry air. The reader is referred to Skamarock et al. (2005) for a complete description of the WRF modeling system.

b. Data assimilation system

Assimilation experiments were conducted using the EnKF algorithm implemented in the Data Assimilation Research Testbed (DART) system developed at the National Center for Atmospheric Research (Anderson et al. 2009). The assimilation algorithm is based on the ensemble adjustment Kalman filter described by Anderson (2001), which processes a set of observations serially and is mathematically equivalent to the ensemble square root filter described by Whitaker and Hamill (2002). DART includes tools that automatically compute temporally and spatially varying covariance inflation values during the assimilation step (Anderson 2007a, 2009). To reduce sampling error resulting from a small ensemble size, horizontal and vertical covariance localization (Mitchell et al. 2002; Hamill et al. 2001; Houtekamer et al. 2005) is performed using a compactly supported fifth-order correlation function following Gaspari and Cohn (1999).

c. Satellite brightness temperature forward model operator

Otkin (2010) implemented a forward radiative transfer model within DART to compute simulated infrared brightness temperatures. CompactOPTRAN, which is part of the National Oceanic and Atmospheric Administration (NOAA) Community Radiative Transfer Model (CRTM), is used to compute gas optical depths for each model layer using simulated temperature and water vapor mixing ratio profiles and climatological ozone data. Ice cloud absorption and scattering properties, such as extinction efficiency, single-scatter albedo, and full scattering phase function, based on Baum et al. (2005) are subsequently applied to each frozen hydrometeor species (i.e., ice, snow, and graupel). A lookup table based on Lorenz–Mie calculations is used to assign the properties for the cloud water and rainwater species. Visible cloud optical depths are calculated separately for the liquid and frozen hydrometeor species following the work of Han et al. (1995) and Heymsfield et al. (2003), respectively, and then converted into infrared cloud optical depths by scaling the visible optical depths by the ratio of the corresponding extinction efficiencies. The surface emissivity over land is obtained from the Seeman et al. (2008) global emissivity database, whereas the water surface emissivity is computed using the CRTM infrared sea surface emissivity model. Finally, the simulated skin

temperature and atmospheric temperature profiles along with the layer gas optical depths and cloud scattering properties are input into the successive order of interaction (SOI) forward radiative transfer model (Heidinger et al. 2006), which is used to compute the simulated brightness temperatures. Previous studies have shown that the forward model produces realistic infrared brightness temperatures for both clear- and cloudy-sky conditions (Otkin and Greenwald 2008; Otkin et al. 2009).

d. Simulated observations

Data from the high-resolution (6 km) "truth" simulation described in section 3 was used to generate simulated observations for the ABI sensor and three conventional observing systems, including radiosondes, the Automated Surface Observing System (ASOS), and the Aircraft Communications Addressing and Reporting System (ACARS). Simulated ABI 8.5-μm infrared brightness temperatures, which are sensitive to cloud-top properties when clouds are present or to the surface when clouds are absent, were computed using the SOI forward radiative transfer model and then averaged to 30-km grid spacing prior to assimilation. Averaged observations were discarded if they contained a mixture of clear and cloudy grid points, thus only completely clear or completely cloudy observations were used during the assimilation experiments. A grid point was considered cloudy if the cloud optical thickness was greater than zero. Simulated 10-m wind speed and direction, 2-m temperature and relative humidity, and surface pressure observations were computed at existing ASOS station locations with vertical profiles of temperature, relative humidity, and horizontal wind speed and direction produced for each radiosonde location. Standard reporting conventions were followed so that each radiosonde profile contains both mandatory level data and significant level data corresponding to features such as temperature inversions and rapid changes in wind speed and direction. Simulated ACARS temperature and wind observations were produced at the same locations as the real pilot reports listed in the Meteorological Assimilation Data Ingest Files for the OSSE case study period. Realistic measurement errors drawn from an uncorrelated Gaussian error distribution and based on a given sensor's accuracy specification were added to each observation.

e. Observation errors

Observation errors used during the assimilation experiments include instrument and representativeness error components. The observation error for the ABI 8.5-μm brightness temperatures was set to 5 K for both clear- and cloudy-sky observations, which is within the error range employed by prior assimilation studies (e.g.,
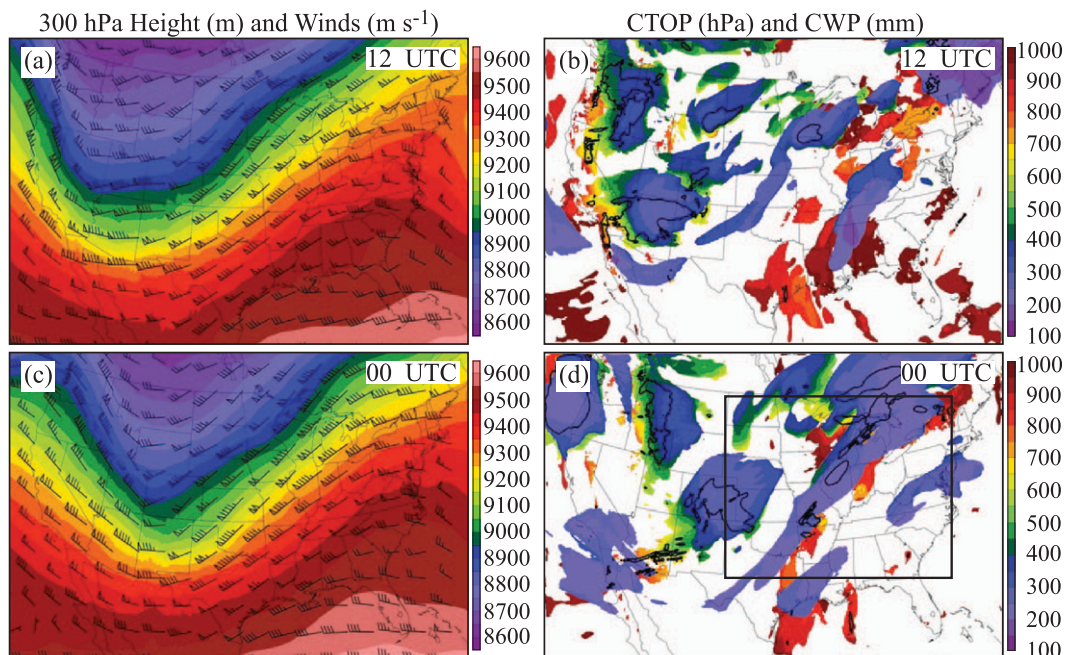
FIG. 1. (a) Simulated 300-hPa geopotential height (m) and winds (m s^{-1}) valid at 1200 UTC 7 Jan 2008. Each wind barb equals 5 m s^{-1}. (b) Simulated cloud-top pressure (hPa; color filled) valid at 1200 UTC 7 Jan 2008. Areas enclosed by the black contour contain a cloud water path greater than 0.4 mm. (c),(d) As in (a),(b), but valid at 0000 UTC 8 Jan 2008. The black rectangle encloses the region used for the forecast verification in section 4f.

Seaman et al. 2010; Otkin 2010). For the conventional observations, the errors were based on those found in the operational dataset from the National Centers for Environmental Prediction. For the ASOS observations, the error was set to 2 K for temperature, 18% for relative humidity, 1.5 hPa for surface pressure, and 2.5 m s^{-1} for the zonal and meridional wind components. Errors of 1.8 K and 3.8 m s^{-1} were used for the ACARS temperature and wind components. The radiosonde errors varied with height and ranged from 0.8–1.2 K for temperature, 1.4–3.2 m s^{-1} for the wind components, and 10%–15% for relative humidity.

3. Truth simulation

A high-resolution truth simulation tracking the evolution of several extratropical weather systems across the contiguous United States was performed using the WRF model. The simulation was initialized at 1200 UTC 6 January 2008 using 20-km Rapid Update Cycle (RUC) model analyses and then integrated for 42 h on a single 798 × 516 gridpoint domain (refer to Fig. 1) containing 6-km horizontal grid spacing and 52 vertical levels. The vertical grid spacing decreased from <100 m in the lowest km to ~500 m at the model top, which was set to 65 hPa. Subgrid-scale processes were parameterized using the Thompson et al. (2008) mixed-phase cloud

microphysics scheme, the Yonsei University (Hong et al. 2006) planetary boundary layer scheme, and the Dudhia (1989) shortwave and Rapid Radiative Transfer Model longwave (Mlawer et al. 1997) radiation schemes. Surface heat and moisture fluxes were calculated using the Noah land surface model. No cumulus parameterization scheme was used.

The evolution of the simulated cloud-top pressure (CTOP), cloud water path (CWP), and 300-hPa height and wind fields from 1200 UTC 7 January to 0000 UTC 8 January 2008 is shown in Fig. 1. Simulated observations from this time period will be assimilated during the experiments presented in section 4. The CTOP corresponds to the atmospheric pressure on the highest model level containing a nonzero hydrometeor mixing ratio whereas the CWP was calculated using the sum of the cloud water, rainwater, ice, snow, and graupel mixing ratios integrated over the entire model column. At 1200 UTC, a broad upper-level trough was located across the western United States (Fig. 1a) with a seasonally strong jet streak (50 m s^{-1}) extending across the central United States. Several large cloudy areas (Fig. 1b) were located within the trough and also along and to the east of a strong surface boundary extending roughly southwest to northeast across the central United States (not shown). By 0000 UTC, the 300-hPa trough had deepened slightly as it slowly moved eastward and encountered a dominant

ridge over the eastern United States (Fig. 1c). Extensive upper-level cloud cover associated with a strong short-wave disturbance was present over the central High Plains while other cloudy areas were located along the Pacific Northwest coast, the northern Rockies, and along the frontal boundary draped across the central United States (Fig. 1d). Predominately clear areas were present over the southeastern United States, northern Mexico, and scattered across the western and central United States.

4. Assimilation results

a. Initial ensemble and model configuration

The assimilation experiments described later in this section begin at 1200 UTC 7 January 2008. Initial conditions valid at this time were created for an 80-member WRF model ensemble using the following procedure, which is identical to that employed by Otkin (2010). First, a preliminary ensemble valid at 0000 UTC 6 January was created using the approach outlined by Torn et al. (2006). With this approach, balanced initial and lateral boundary perturbations were added to 40-km North American Mesoscale (NAM) model analyses for each ensemble member using covariance information provided by the WRF-Var data assimilation system. This ensemble was then integrated for 24 h to increase the ensemble spread. Last, simulated ASOS, ACARS, and radiosonde observations from the truth simulation were assimilated during the next 12 h to produce an initial ensemble for the assimilation experiments described later in this section that contain flow-dependent covariance structures that are more representative of the atmospheric conditions in the truth simulation.

Assimilation experiments were performed for the same geographic domain as the truth simulation, but contained 18-km horizontal grid spacing and 37 vertical levels in order to better represent an operational setting. Unlike the truth simulation, the Kain and Fritsch (1990, 1993) subgrid-scale cumulus parameterization scheme was employed during the assimilation experiments. Different initialization datasets, grid resolutions, and parameterization schemes were chosen for the assimilation experiments to limit the risk of performing "identical twin" experiments.

In the remainder of this section, results from four assimilation experiments will be compared to data from the truth simulation. The experiments are designed to evaluate the impact of the horizontal localization radius on the analysis accuracy and short-range model forecasts when assimilating 8.5-μm brightness temperatures. Simulated conventional observations were the only observations assimilated during the Control case, while both conventional

observations and clear- and cloudy-sky 8.5-μm brightness temperatures were assimilated during the other cases. When assimilating 8.5-μm observations, the horizontal localization radius was set to 100, 200, and 300 km during the HLOC-100KM, HLOC-200KM, and HLOC-300KM cases, respectively. For the conventional observations, sensitivity tests showed that the best results were obtained with a 6-km vertical localization radius, and horizontal localization radii of 400 km for surface pressure and relative humidity and 600 km for temperature and wind. Vertical covariance localization was not used for the brightness temperature observations since they are sensitive to broad layers of the atmosphere. Simulated radiosonde observations were assimilated at 0000 and 1200 UTC, whereas all other observation types were assimilated once per hour from 1200 UTC 7 January to 0000 UTC 8 January. Prognostic fields contained in the model state vector that are updated during each assimilation cycle include the temperature, water vapor mixing ratio, horizontal and vertical wind components, surface pressure, number concentration of ice, and the mixing ratios for cloud water, rainwater, pristine ice, snow, and graupel. The time and spatially varying covariance inflation scheme developed by Anderson et al. (2009) was also used during each experiment.

b. Time series error analysis

As a first step in evaluating the impact of the observations on the analysis accuracy, Fig. 2 shows the temporal evolution of the prior and posterior root-mean-square error (RMSE) and bias for the ABI 8.5-μm band for each assimilation cycle during the 12-h assimilation period. Output from the truth simulation was coarsened to 18-km grid spacing and then statistics were computed with respect to the clear and cloudy grid points in the truth simulation. Data from the outermost 20 grid points were not used. Overall, the RMSE and bias were much smaller during the brightness temperature assimilation cases. For the clear-sky grid points (Fig. 2b), the RMSE was reduced by 4–5 K after the first assimilation cycle, due in part to a large reduction in the negative bias present in the initial ensemble (Fig. 2d). Nearly constant errors occurred during the remainder of the assimilation period. Assimilation of the brightness temperature observations also lowered the RMSE and bias for the cloudy grid points (Figs. 2a,c), though the improvement relative to the Control case decreased slightly by the end of the assimilation period. Comparison of the brightness temperature assimilation cases shows that the larger horizontal localization radius used during the HLOC-300KM case initially exerted a stronger positive influence on the cloudy-sky grid points, but that this impact decreased with time and was similar to the other cases by
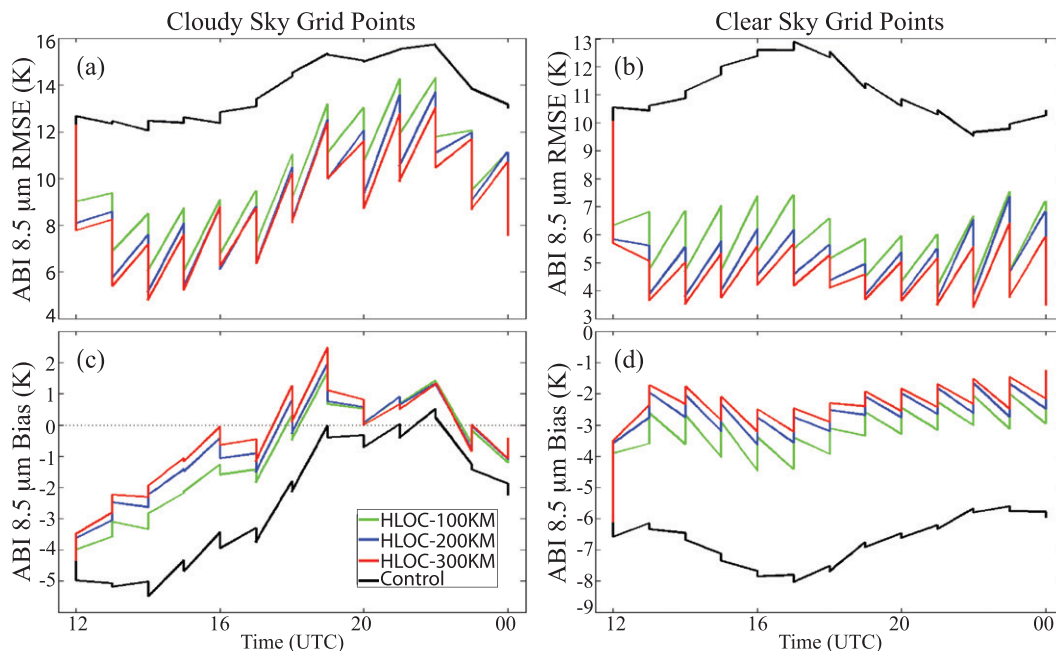
FIG. 2. Time evolution of the ensemble mean forecast and analysis (sawtooth pattern) ABI 8.5-μm brightness temperature RMSE (K) from 1200 UTC 7 Jan to 0000 UTC 8 Jan 2008 computed with respect to the (a) cloudy- and (b) clear-sky grid points in the truth simulation. (c),(d) As in (a),(b), but for the time evolution of the ABI 8.5-μm brightness temperature bias (K). Results are shown for the HLOC-100KM (green), HLOC-200KM (blue), HLOC-300KM (red), and Control (black) experiments.

0000 UTC. Larger and more consistent error reductions occurred for the clear-sky grid points when a larger localization radius was used. The ratio between the ensemble spread and the RMSE for the 8.5-μm brightness temperature observations decreased slightly with increasing localization radius (not shown), which indicates that the ensemble spread was reduced when a larger localization radius was used. This could have an adverse affect on filter performance over longer assimilation periods.

Figure 3 shows the evolution of the prior and posterior bias and RMSE for the CWP computed with respect to the cloudy and clear grid points in the truth simulation. Similar to Fig. 2, applying a larger localization radius to the 8.5-μm brightness temperature observations leads to slightly smaller RMSE after the first assimilation cycle for both clear- and cloudy-sky grid points (Figs. 3a,b). The superior performance continues during most of the assimilation period for the clear-sky grid points with the HLOC-300KM case containing the smallest bias and RMSE by 0000 UTC. For the cloudy grid points, however, the RMSE grows more rapidly during the HLOC-300KM case so that the errors become larger after 1600 UTC and are nearly 15% larger than the HLOC-100KM case by the end of the assimilation period. All three brightness temperature assimilation cases

contain consistently smaller errors for the clear-sky grid points; however, larger biases occurred for the cloudy grid points during most of the assimilation period (Fig. 3c), which indicates that cloudy infrared observations have the tendency to add too much cloud condensate to the column. The different performance for the clear and cloudy grid points suggests that the smaller-scale structure apparent in many cloud fields may require a smaller localization radius to achieve optimal results. For instance, cloud properties can vary quickly over short distances so a smaller localization radius limits the spread of information from individual cloudy observations that may not be totally representative of the larger cloud structure (such as a thunderstorm within a cirrus cloud shield) and also helps to preserve smaller cloud features when surrounded by clear observations (e.g., Polkinghorne et al. 2010). Errors in the model parameterized cloud microphysics may also contribute to the different performance.

Figure 4 shows the evolution of the prior and posterior bias and RMSE for the column-integrated precipitable water content computed with respect to the clear and cloudy grid points in the truth simulation. Overall, the assimilation of 8.5-μm brightness temperatures had a minimal impact on the RMSE during the first several assimilation cycles relative to the Control case (Figs. 4a,b);
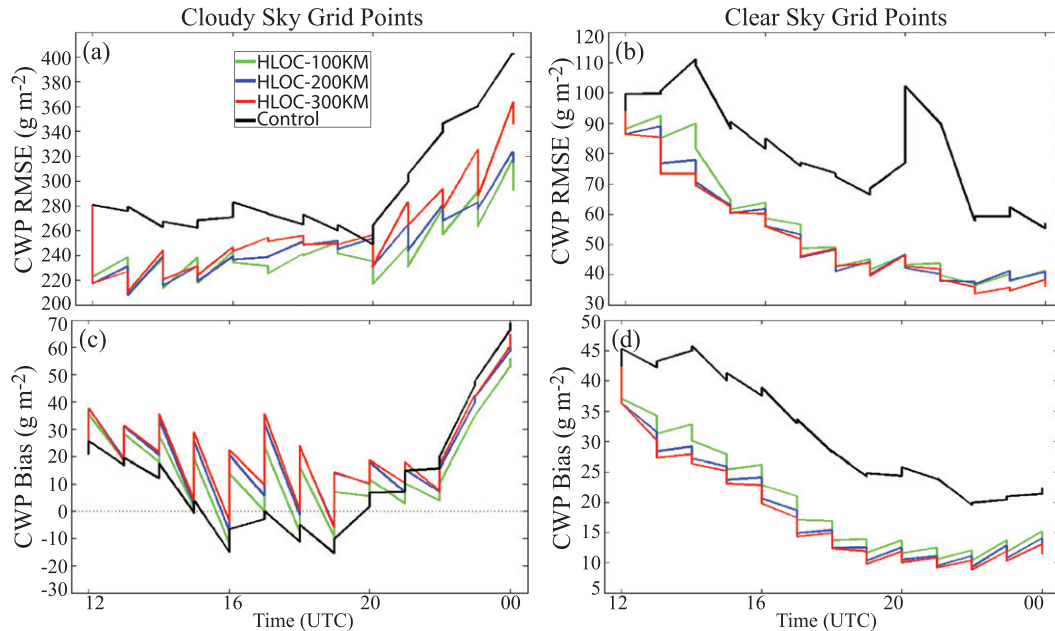
FIG. 3. Time evolution of the ensemble mean forecast and analysis (sawtooth pattern) CWP RMSE (g m^{-2}) from 1200 UTC 7 Jan to 0000 UTC 8 Jan 2008 computed with respect to the (a) cloudy- and (b) clear-sky grid points in the truth simulation. (c),(d) As in (a),(b), but for the time evolution of the CWP bias (g m^{-2}). Results are shown for the HLOC-100KM (green), HLOC-200KM (blue), HLOC-300KM (red), and Control (black) experiments.

however, the performance of each case started to diverge by 1800 UTC with the largest errors occurring during the HLOC-300KM case. The RMSE consistently decreased as the localization radius was reduced to 100 km, with the improvements increasing with time. The HLOC-100KM case was the only one that contained smaller errors than the Control case, which suggests that the covariances between the infrared observations and the water vapor field may be noisy at larger separation distances and therefore necessitates using a smaller localization radius for this combination of observations and state variables. Last, the initial ensemble was characterized by a large dry bias (Figs. 4c,d) that the observations were unable to correct. For the cloudy-sky grid points, the bias was slightly improved by 0000 UTC during the HLOC-100KM and HLOC-200KM cases; however, the bias steadily worsened with time for the clear-sky grid points and consistently increased with increasing localization radius. The notable drying inferred by the increasing negative bias shows that the clear-sky 8.5-μm observations exert a strong influence on the moisture field. Future work will be necessary to determine if the anomalous drying is due to errors in the background error covariance field when both the observation and ensemble members are clear or whether it is due to erroneous drying of the atmosphere instead of the removal of cloud condensate when clouds are present in the ensemble.

c. Regional cloud water path analysis

To further investigate the impact of brightness temperature assimilation on the cloud analysis, Fig. 5 shows the 8.5-μm brightness temperature and CWP mean analysis increments (MAI) and the differences between the posterior ensemble mean CWP and the truth simulation after the first assimilation cycle at 1200 UTC. The CWP and 8.5-μm brightness temperatures from the truth simulation and the prior ensemble mean are also shown. In the truth simulation (Figs. 5a,b), thick cloud cover and cold 8.5-μm brightness temperatures are present over southern Minnesota and Wisconsin and downstream of the Big Horn Mountains in northern Wyoming and the Front Range of Colorado with several areas of low and midlevel clouds containing less cloud condensate scattered across the rest of the region. Colder brightness temperatures and more extensive cloud cover were present in the prior ensemble mean (Figs. 5c,d), which is primarily due to differences in the strength and location of the cloud features in each ensemble member. Comparison of the Control (Figs. 5e–g) and brightness temperature assimilation (Figs. 5h–p) cases reveals substantial differences in the magnitude and structure of the CWP and 8.5-μm brightness temperature increments when infrared observations are assimilated. For instance, much larger positive brightness temperature increments consistent

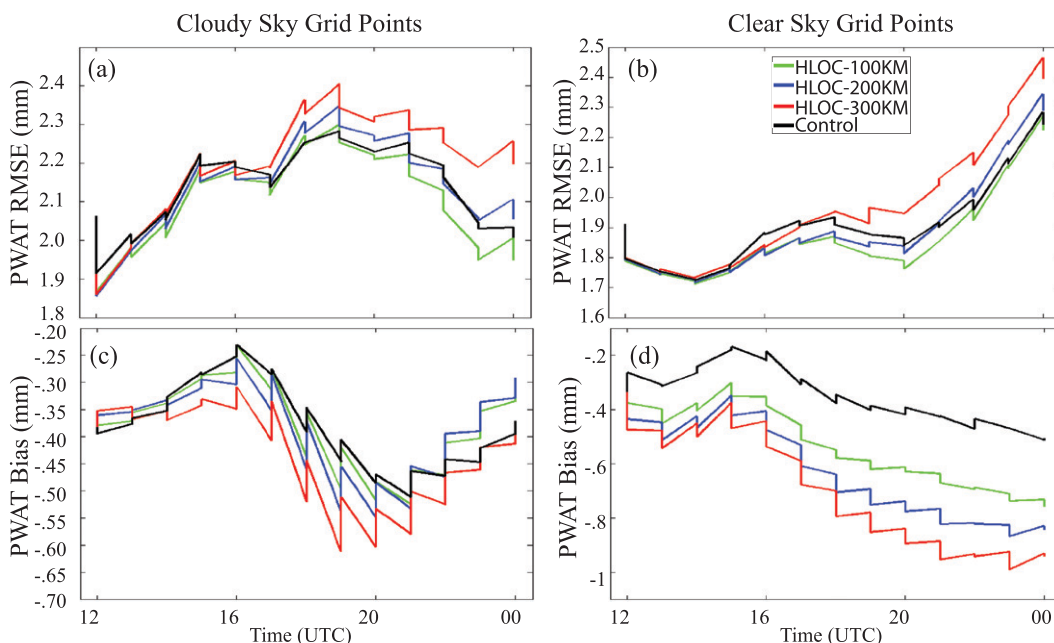Cloudy Sky Grid Points   Clear Sky Grid Points

FIG. 4. Time evolution of the forecast and analysis (sawtooth pattern) precipitable water (PWAT) RMSE (mm) from 1200 UTC 7 Jan to 0000 UTC 8 Jan 2008 computed with respect to the (a) cloudy- and (b) clear-sky grid points in the truth simulation. (c),(d) As in (a),(b), but for the time evolution of the PWAT bias (mm). Results are shown for the HLOC-100KM (green), HLOC-200KM (blue), HLOC-300KM (red), and Control (black) experiments.

with the removal of cloud condensate from some or all of the ensemble members occurred across the central Plains and Great Lakes regions when 8.5-μm brightness temperatures were assimilated. The influence of the localization radius is apparent over extreme western Iowa, where the spatial extent of the positive CWP MAI is progressively smaller as the localization radius increases. This effect occurs because a larger localization radius allows the clear-sky observations that predominate across this area (Fig. 5a) to more easily overcome the positive CWP increments induced by the conventional observations (Fig. 5f). Large differences also occurred within the elongated cloud feature extending downstream of the Bighorn Mountains where the prior ensemble mean had greatly underestimated the CWP. The relative lack of conventional observations across this region and their insensitivity to the cloud field limited their ability to improve the CWP. The greater sensitivity of the 8.5-μm brightness temperatures, however, allowed them to exert a much larger positive influence on the cloud field even though the 8.5-μm brightness temperature MAI were not particularly large.

d. Vertical cross sections

In this section, the impact of the observations on the vertical distribution of cloud condensate and other

thermodynamic fields will be more closely examined for the cloud feature extending downstream of the Bighorn Mountains (refer to Fig. 5a for the cross-section location). Figure 6 shows vertical cross sections of total cloud hydrometeor (QALL; sum of cloud water, rainwater, ice, snow, and graupel) and water vapor (Q_V) mixing ratios from the truth simulation and prior ensemble mean at 1200 UTC along with the MAI and posterior ensemble mean error for each assimilation case. Comparison with the truth simulation (Fig. 6a) reveals that the prior ensemble mean (Fig. 6b) contains several large errors, including a severe underestimation of the amount of cloud condensate immediately northeast of the mountains, the presence of erroneously dry low-level air in the same region, and a lack of dry midlevel air above the shallow moist layer farther to the northeast (between 550 and 750 km). The large errors were primarily due to differences in the initialization datasets and model resolutions used for the truth simulation and assimilation experiments. During the Control case (Figs. 6c,d), the conventional observations had little appreciable impact on the QALL and Q_V errors close to the mountains; however, large-scale drying (moistening) in the lower (middle) troposphere slightly reduced the Q_V errors (up to 15%) between 600 and 750 km. For the brightness temperature assimilation cases (Figs. 6e–j), two narrow plumes of cloud condensate were added near
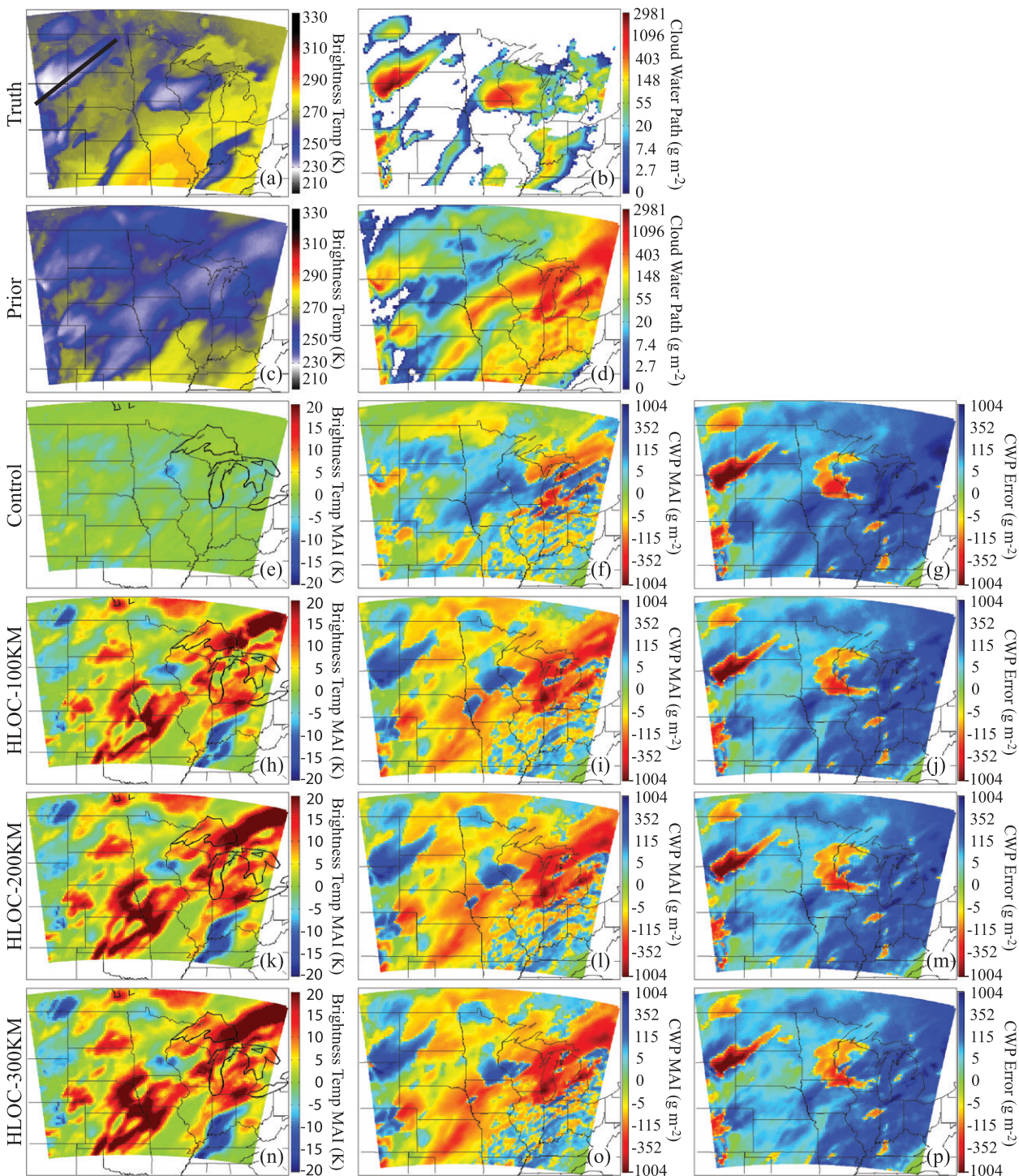
FIG. 5. (a) Simulated ABI 8.5-μm brightness temperatures (K) and (b) CWP (g m^{-2}) from the truth simulation. The location of the cross sections in Figs. 6 and 7 is indicated by the black line. (c),(d) As in (a),(b), but for the prior ensemble mean. (e) 8.5-μm brightness temperature mean analysis increment (K), (f) CWP mean analysis increment (g m^{-2}), and (g) CWP mean error (g m^{-2}) for the Control simulation. (h)–(j) As in (e)–(g), but for the HLOC-100KM case. (k)–(m) As in (e)–(g), but for the HLOC-200KM case. (n)–(p) As in (e)–(g), but for the HLOC-300KM case. All images valid at 1200 UTC 8 Jan 2008.
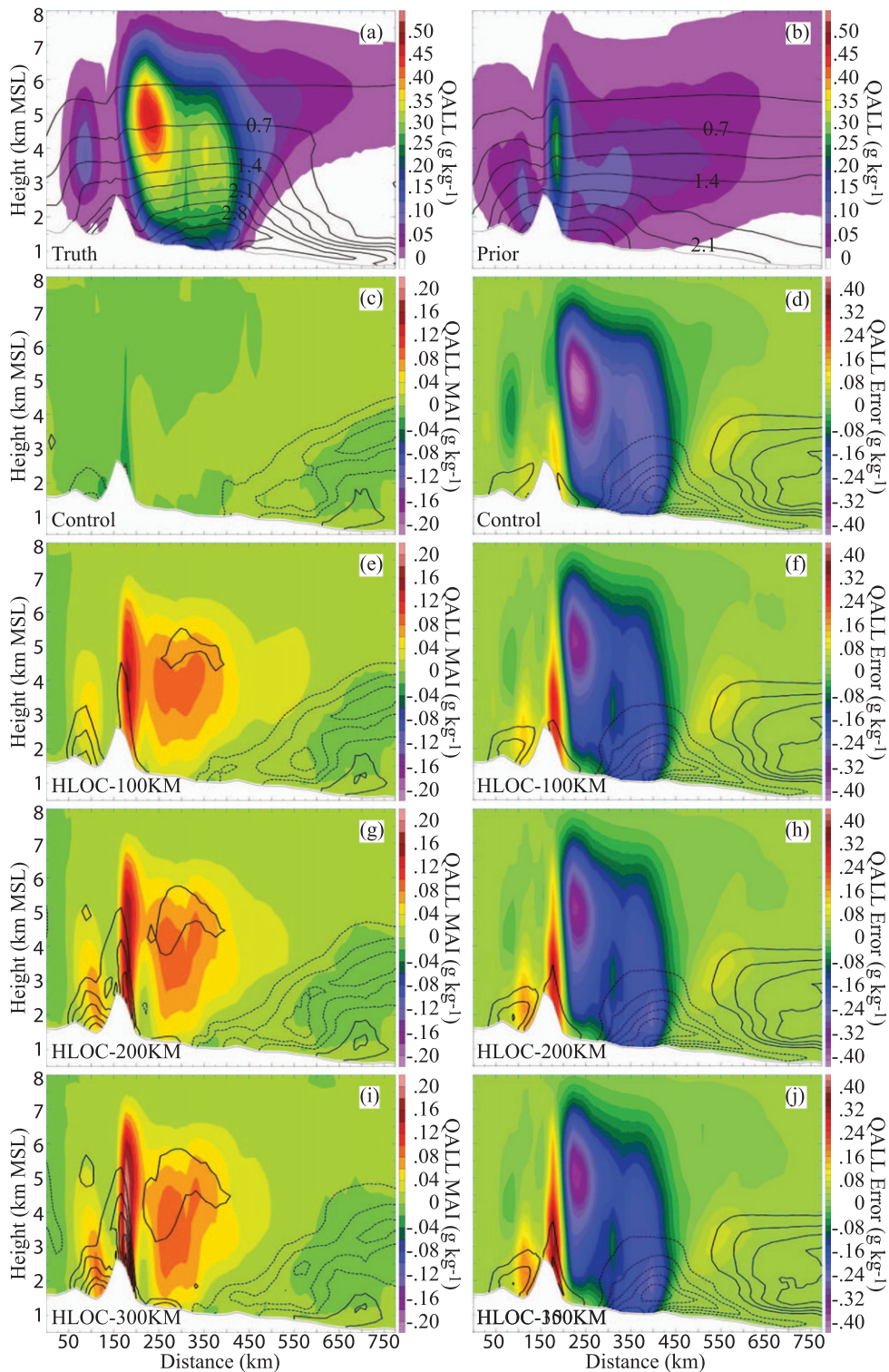
FIG. 6. Vertical cross section of total cloud mixing ratio (sum of cloud water, rainwater, ice, snow and graupel) (g kg^{-1}; color fill) and water vapor mixing ratio (g kg^{-1}; contours) from the (a) truth simulation and (b) prior ensemble mean valid at 1200 UTC 7 Jan 2008. (c) Vertical cross section of total cloud mixing ratio (g kg^{-1}) and water vapor mixing ratio (g kg^{-1}) mean analysis increment from the Control case. Water vapor mixing ratio is contoured every 0.06 g kg^{-1} with negative values dashed and zero contour omitted. (d) Vertical cross section of total cloud mixing ratio (g kg^{-1}) and water vapor mixing ratio (g kg^{-1}) errors

the mountains with a larger region of positive QALL increments located between 200 and 450 km. The magnitude of the increments tends to increase with increasing localization radius, which was beneficial downstream of the mountains, but lead to larger QALL errors within the narrow cloud plumes. Although the brightness temperatures had minimal impact on the Q_V errors away from the mountains, the large positive Q_V increments near the mountains introduced a wet bias in the lower troposphere that was largest for the HLOC-300KM case.

Vertical cross sections of potential temperature and along-cross-section wind speed from the truth simulation and prior ensemble mean at 1200 UTC, and the corresponding MAI and posterior ensemble mean error for each assimilation case are shown in Fig. 7. Comparison with the truth simulation (Fig. 7a) reveals that the prior ensemble mean (Fig. 7b) contains a lower tropopause and stronger upper-level winds extending northeast from the mountains, cooler (warmer) temperatures below (above) 7 km MSL associated with the lower tropopause, and much weaker upslope northeasterly winds below 5 km MSL. The weaker upslope flow in the prior ensemble likely contributed to the lower QALL and Q_V mixing ratios seen in Fig. 6b. When conventional observations were assimilated during the Control case (Figs. 7c,d), the upper-level temperature errors southwest of the mountains were reduced by up to 1 K with smaller improvements in the temperature and wind analyses farther to the northeast. Much larger analysis increments occurred when 8.5-μm brightness temperatures were assimilated (Figs. 7e–j), which generally resulted in a more accurate analysis, especially for wind as a result of the presence of stronger northeasterly flow at most levels. Varying the localization radius for the infrared observations had a minimal impact on the shape of the analysis increments; however, their magnitude greatly increased as the localization radius increased from 100 to 300 km. For instance, the maximum wind speed increment near 7 km MSL increased from −3 m s^{-1} in the HLOC-100KM case to −7 m s^{-1} in the HLOC-300KM case, while the maximum temperature increment above this level increased from −1.6 to −2.4 K. Warming in the middle troposphere also increased from 0.4 to 1.1 K for these cases. The

larger MAI during the HLOC-300KM case generally resulted in the most accurate analysis after the first assimilation cycle, which is consistent with the results presented in section 4b.

e. Final analysis accuracy

The accuracy of the final analysis obtained after 12 h of assimilation is assessed in this section. Figure 8 shows vertical profiles of bias and RMSE for QALL computed with respect to the clear and cloudy grid points in the truth simulation. The statistics were calculated for each case using data from the posterior ensemble mean at 0000 UTC 8 January, excluding the outermost 20 grid points of the model domain. Overall, the cloud analysis was greatly improved when 8.5-μm brightness temperatures were assimilated simultaneously with the conventional observations. For instance, the RMSE for the brightness temperature assimilation cases is much lower than the Control case for both clear and cloudy grid points (Figs. 8b,d), with the largest error reductions occurring in the middle and upper troposphere similar to what was shown in Otkin (2010). The smaller impact of the infrared observations on the low-level clouds is likely due to two reasons. First, for optically deep clouds or for multilayer cloud situations, infrared observations are not sensitive to the lower portion of the cloud field, thereby limiting their direct impact on the cloud analysis. Second, in the absence of upper-level clouds, the thermal contrast between a low-level cloud and the surface will be much smaller than between an upper-level cloud and the surface, which will result in smaller analysis increments unless the observation errors can be reduced for clear-sky observations and for those containing low-level clouds. Comparison of the brightness temperature assimilation cases reveals that similar errors occurred for the clear-sky grid points; however, the QALL errors consistently decreased with decreasing localization radius for the cloudy-sky grid points. These results are consistent with those shown in Fig. 3 and again suggest that different localization radii may be necessary to account for differences in the representative scale of clear and cloudy observations.

Vertical profiles of bias and RMSE for temperature, water vapor mixing ratio, and vector wind speed computed with respect to the clear and cloudy grid points in

←

from the Control case computed by subtracting the posterior ensemble mean from truth. Water vapor mixing ratio is contoured every 0.25 g kg^{-1} with negative values dashed and the zero contour omitted. (e),(f) As in (c),(d), but for HLOC-100KM case. (g),(h) As in (c),(d), but for HLOC-200KM case. (i),(j) As in (c),(d), but for HLOC-300KM case.
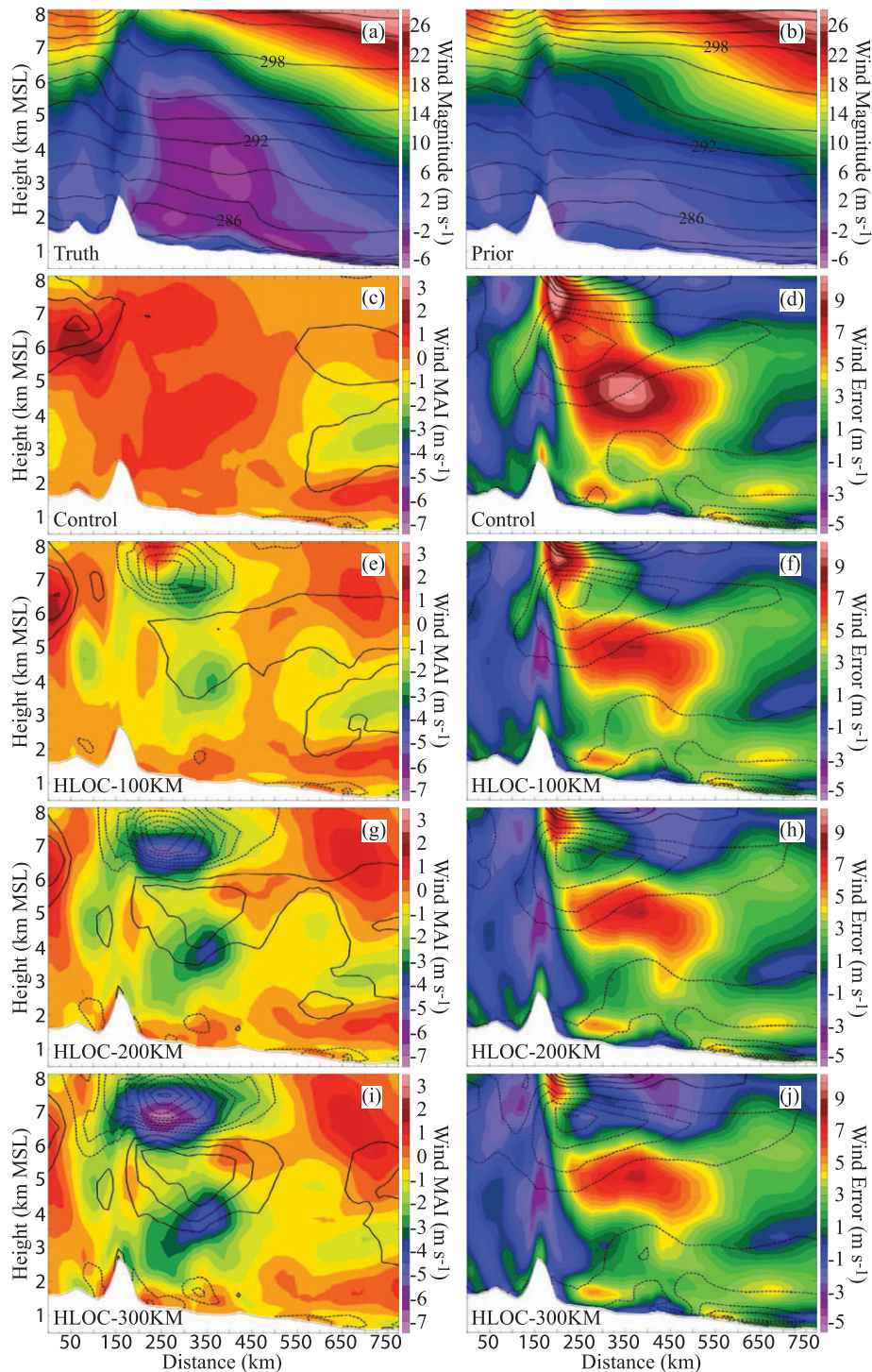
FIG. 7. Vertical cross section of along-cross-section wind speed (m s^{-1}; color fill) and potential temperature (K; contours) from the (a) truth simulation and (b) prior ensemble mean valid at 1200 UTC 7 Jan 2008. (c) Vertical cross section of potential temperature (K) and wind (m s^{-1}) mean analysis increment from the Control case. Temperature is contoured every 0.3 K with negative values dashed and zero contour omitted. (d) Vertical cross section of potential temperature (K) and wind (m s^{-1}) errors from the Control case computed by subtracting the posterior ensemble mean from truth. Temperature is contoured every 1 K with negative values dashed and zero contour omitted. (e),(f) As in (c),(d), but for HLOC-100KM case. (g),(h) As in (c),(d), but for HLOC-200KM case. (i),(j) As in (c),(d), but for HLOC-300KM case.
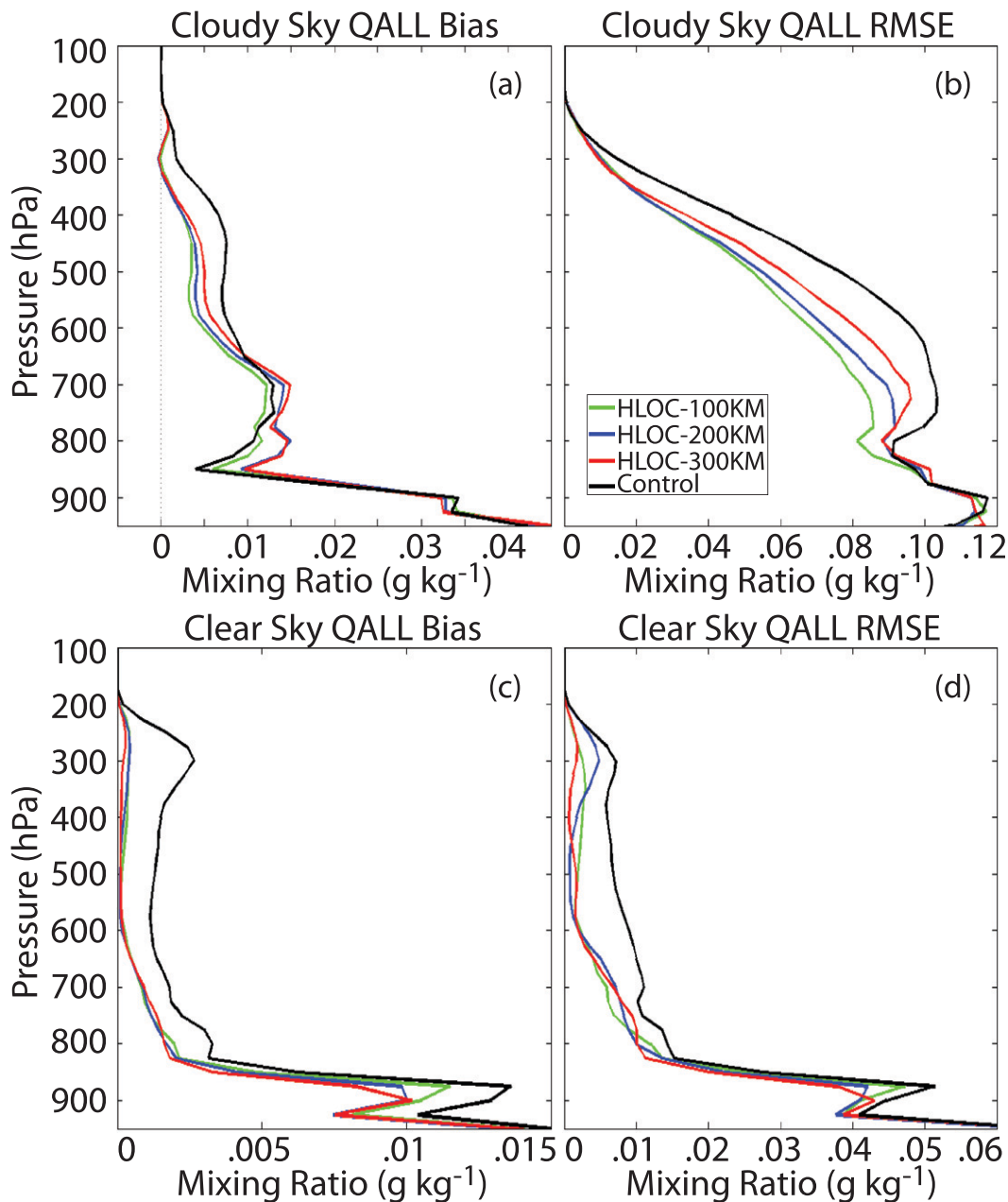
FIG. 8. Vertical profiles of (a) bias and (b) RMSE for the total hydrometeor mixing ratio (g kg^{-1}; sum of cloud water, rainwater, cloud ice, snow, and graupel) for cloudy grid points. The profiles were computed using data from the posterior ensemble mean at 0000 UTC 8 Jan 2008. (c),(d) As in (a),(b), but for clear grid points. Results are shown for the HLOC-100KM (green), HLOC-200KM (blue), HLOC-300KM (red), and Control (black) experiments, with the statistics calculated with respect to the cloudy and clear grid points in the truth simulation.

the truth simulation are shown in Fig. 9. Close inspection shows that the assimilation of 8.5-μm brightness temperatures improved the temperature analysis in the middle troposphere for the cloudy grid points; however, larger errors occurred elsewhere (Figs. 9a,b). For the clear-sky grid points (Figs. 9c,d), the temperature errors were higher for most levels, though some improvements did occur in

the lower troposphere during the HLOC-100KM case. Much larger errors were introduced to the water vapor analysis when brightness temperatures were assimilated (Figs. 9e–h), primarily due to the presence of a wet (dry) bias for the cloudy (clear) grid points. Last, although the wind analysis (Figs. 9i,j) was characterized by slightly smaller errors in the middle troposphere for the cloudy
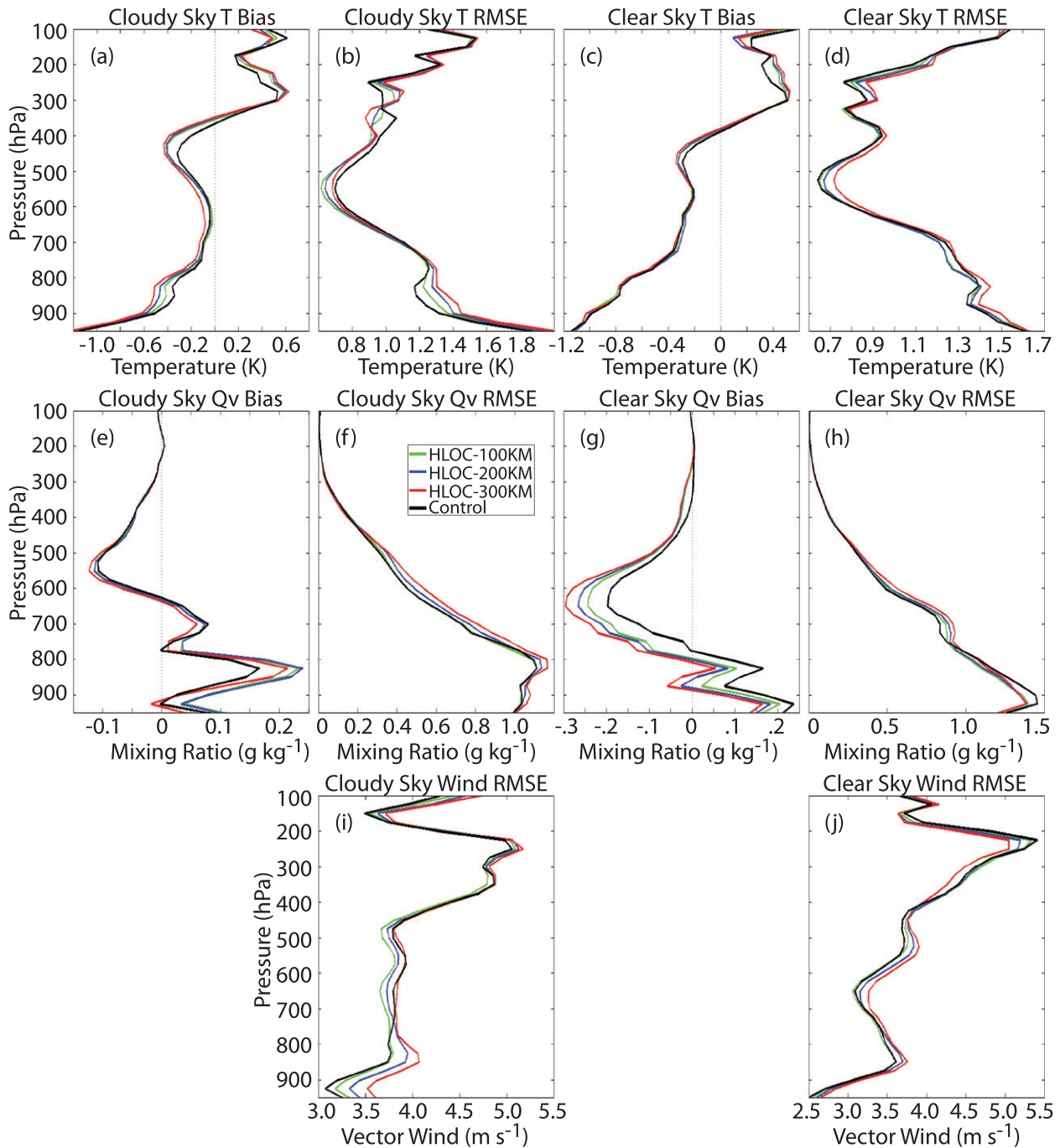
FIG. 9. Vertical profiles of (a) bias and (b) RMSE for temperature (K) for cloudy grid points. The profiles were computed using data from the posterior ensemble mean at 0000 UTC 8 Jan 2008. (c),(d) As in (a),(b), but for clear grid points. (e)–(h) As in (a)–(d), but for water vapor mixing ratio (g kg^{-1}). (i) As in (b), but for vector wind (m s^{-1}). (j) As in (d), but for vector wind (m s^{-1}). Results are shown for the HLOC-100KM (green), HLOC-200KM (blue), HLOC-300KM (red), and Control (black) experiments, with the statistics calculated with respect to the cloudy and clear grid points in the truth simulation.

grid points and in the upper troposphere for the clear grid points, some degradation occurred at other levels. In general, the RMSE for these variables was similar to or slightly better than the Control case only when the

localization radius was reduced to 100 km, while the greatest degradation tended to occur for both clear and cloudy grid points when a larger localization radius was used. Combining these results with Fig. 8 indicates

that although the infrared observations were able to consistently improve the cloud analysis regardless of the length of the localization radius, it was necessary to use a smaller localization radius to maintain or improve the accuracy of the thermodynamic and moisture analyses relative to the Control case. Future work will be necessary to more fully explore the sensitivity of the analysis accuracy to changes in the ensemble size and the spatial density of the assimilated infrared observations.

f. Forecast impact

To assess the impact of the observations on the short-range model forecast skill, 6-h ensemble forecasts were performed for each case using the final ensemble analyses from 0000 UTC 8 January. Vertical profiles of bias and RMSE for temperature, water vapor mixing ratio, and vector wind speed at the 1-, 3-, and 6-h forecast times are shown in Fig. 10. Data from the ensemble mean for the subdomain shown in Fig. 2 were used to compute the statistics. In general, the thermodynamic errors are larger for the brightness temperature assimilation cases, but tend to decrease with decreasing localization radius and are much closer to the more accurate Control case during the HLOC-100KM case. The poorer forecast performance during these cases is consistent with the generally less accurate moisture and thermodynamic analyses at the end of the assimilation period (Fig. 9).

Figure 11 shows the temporal evolution of the bias and RMSE for the 8.5-μm brightness temperatures, cloud-top pressure, ice water path (IWP), and liquid water path (LWP). Overall, the positive impact of the infrared observations decreases rapidly during the forecast period and converges with the Control case by 0600 UTC for the cloud-top pressure and 8.5-μm brightness temperatures and by 0200 UTC for the IWP and LWP. The corresponding mean absolute error statistics (not shown) are consistently smaller for the brightness temperature assimilation cases during the entire 6-h forecast period, which illustrates that assimilation of infrared observations helps constrain the evolution of cloud-sensitive fields more than conventional observations alone, but that much larger errors for some grid points result in a higher RMSE during later forecast periods. The rapid increase in the IWP and LWP errors indicates that improvements in the final cloud analysis (Fig. 8) quickly disappear, possibly due to the less accurate moisture, temperature, and wind analyses at end of the assimilation period (Fig. 9) and the subsequently larger errors during the forecast period (Fig. 10). If the moisture and thermodynamic forcing controlling the cloud evolution are not improved, then it is difficult to maintain the beneficial changes made to the final cloud analysis. Last, comparison of the brightness

temperature assimilation cases shows that the RMSE tended to decrease for these cloud-sensitive variables as the localization radius was increased.

5. Discussion and conclusions

In this study, a regional-scale OSSE was used to examine how changes in the horizontal covariance localization radius employed during the assimilation of clear- and cloudy-sky infrared brightness temperature observations impacts the accuracy of atmospheric analyses and short-range model forecasts. The OSSE case study tracked the evolution of several extratropical weather systems and the associated cloud features that occurred across the contiguous United States during 7–8 January 2008. A high-resolution "truth" simulation containing realistic cloud, moisture, and thermodynamic properties was performed using the WRF model. Data from this simulation were used to generate synthetic ABI 8.5-μm brightness temperatures and conventional radiosonde, surface, and aircraft pilot observations. Realistic errors based on a given sensor's accuracy specifications drawn from a Gaussian error distribution were added to each observation. Four assimilation experiments were conducted using the EnKF algorithm in the DART assimilation system. Conventional observations were assimilated during the Control experiment, whereas both conventional and clear- and cloudy-sky 8.5-μm brightness temperature observations were assimilated during the other cases. For the cases with brightness temperature assimilation, the horizontal localization radius was set to 100, 200, and 300 km, respectively, for the 8.5-μm observations. All observations were assimilated once per hour during a 12-h period, with 6-h ensemble forecasts performed using the final ensemble analyses at the end of the assimilation period.

Overall, the results indicate that assimilating 8.5-μm brightness temperatures improves the analysis and forecast accuracy for variables sensitive to the cloud field, but has the tendency to degrade other fields. Comparison of the brightness temperature assimilation cases reveals that the horizontal localization radius strongly influences the assimilation performance for both clear- and cloudy-sky grid points. After the first assimilation cycle, large differences were evident in the magnitude and structure of the CWP increments across the central United States and downwind of the Rocky Mountains. The influence of the localization radius was most apparent over western Iowa, where a larger radius allowed the clear-sky infrared observations that predominated across the region to overcome the erroneous positive CWP increments induced by the conventional observations. Vertical cross sections through the elongated cloud feature extending
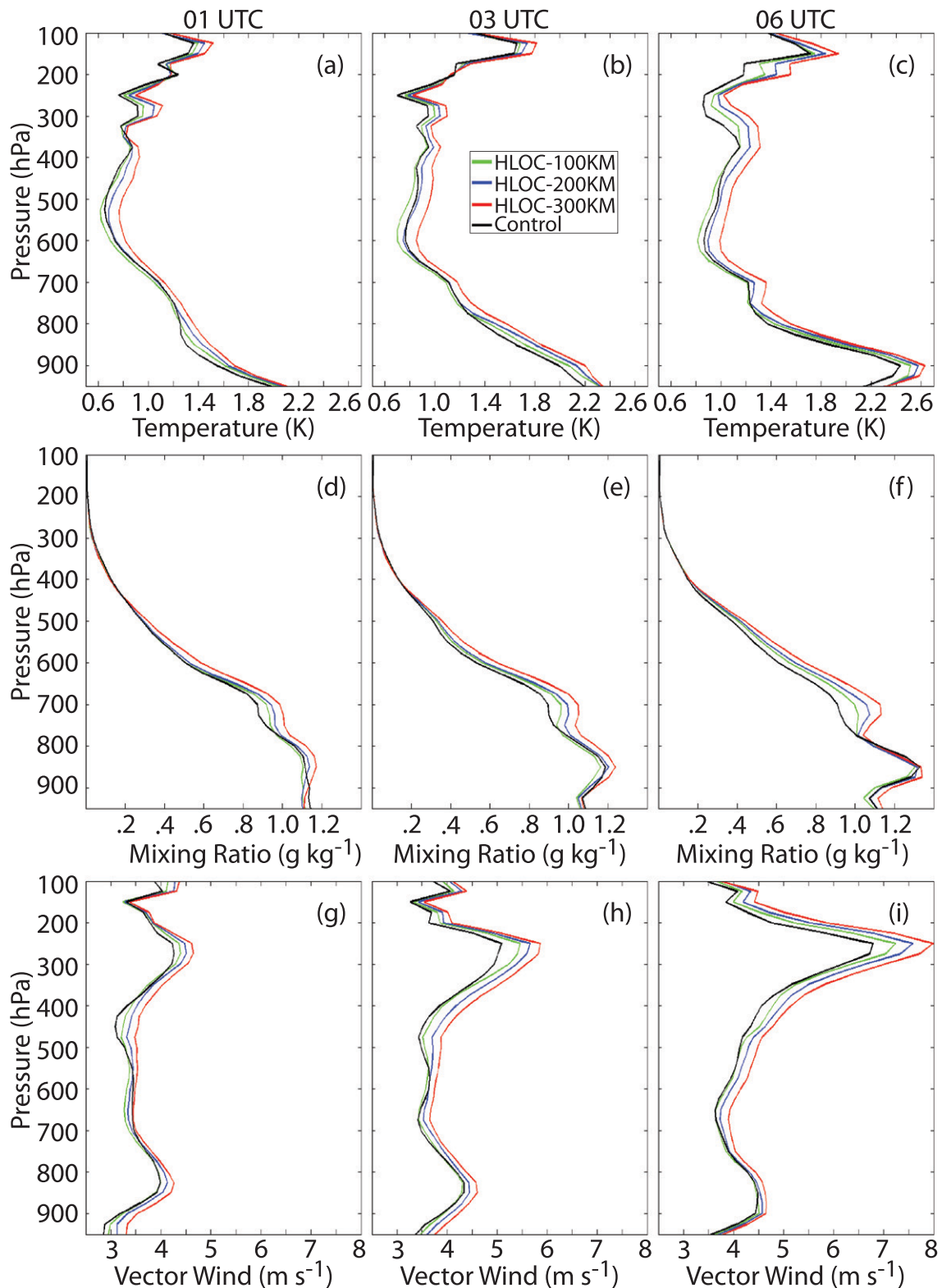
FIG. 10. Temperature forecast RMSE (K) profiles valid at (a) 0100, (b) 0300, and (c) 0600 UTC 8 Jan 2008. (d)–(f) As in (a)–(c), but for water vapor mixing ratio (g kg^{-1}). (g)–(i) As in (a)–(c), but for vector wind (m s^{-1}). Statistics were computed using data from the ensemble mean. Results are shown for the HLOC-100KM (green), HLOC-200KM (blue), HLOC-300KM (red), and Control (black) experiments.

FIG. 11. Time evolution of the forecast RMSE from 0000 UTC 8 Jan 2008 (forecast hour 0) to 0600 UTC 8 Jan 2008 for (a) ABI 8.5-μm brightness temperatures (K), (b) cloud-top pressure (hPa), (c) IWP (g m^{-2}), and (d) LWP (g m^{-2}), computed using data from the ensemble mean. Results are shown for the HLOC-100KM (green), HLOC-200KM (blue), HLOC-300KM (red), and Control (black) experiments.
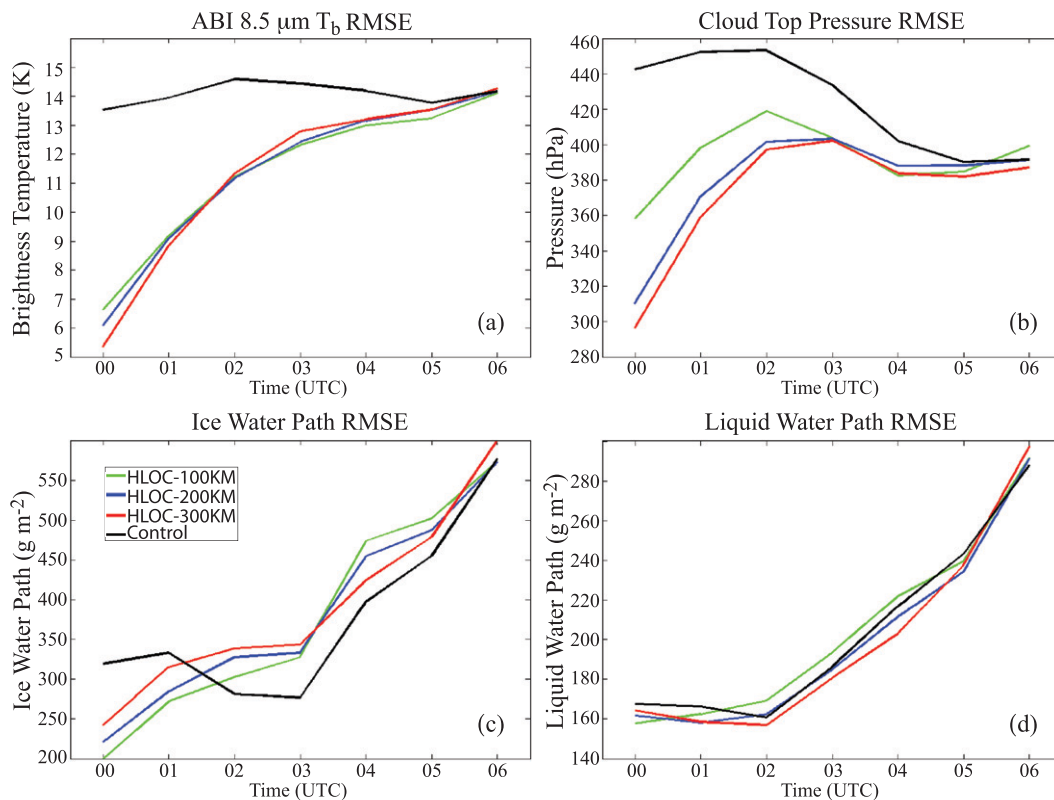
downstream of the Big Horn Mountains showed that much larger analysis increments occurred for the cloud and thermodynamic fields when 8.5-μm observations were assimilated. Varying the localization radius had little impact on the shape of the analysis increments; however, their magnitude consistently increased with increasing localization radius. Although the larger analysis increments during the HLOC-300KM case lead to the most accurate analysis after the first assimilation cycle, the superior performance disappeared for most variables by the end of the assimilation period. For instance, errors in the water vapor, temperature, and wind fields generally decreased with decreasing localization radius and were similar to or even slightly better than the Control case only when the localization radius was reduced to 100 km. Much larger improvements occurred in the cloud analysis during the brightness temperature assimilation experiments, with the smallest errors obtained for the clear (cloudy) grid points when a larger (smaller) localization radius was used. These results suggest that to account for differences in their representative scales, it may be necessary to use different localization radii when assimilating clear and cloudy

infrared observations. Future work will be necessary to determine if this behavior is caused by different correlation lengths between the unobserved fields and the clear and cloudy infrared observations.

Short-range ensemble forecasts were subsequently performed for each case using the final analyses at the end of the 12-h assimilation period. Overall, the temperature, moisture, and wind errors were larger during the brightness temperature assimilation cases, which is consistent with the less accurate moisture and thermodynamic analyses at 0000 UTC. These errors tended to decrease with decreasing localization radius and were much closer to the more accurate Control case during the HLOC-100KM case. The large positive impact of the infrared observations on the cloud analysis diminished rapidly during the forecast period and was similar to the Control case after several hours, which indicates that it is difficult to maintain beneficial changes to the cloud analysis if the corresponding moisture and thermodynamic fields controlling the cloud evolution are not simultaneously improved. In summary, the analysis and forecast results show that although the assimilation of infrared observations consistently improves the cloud

field regardless of the length of the localization radius, it may be necessary to use a smaller radius to improve the accuracy of the moisture and thermodynamic fields. The inability of the infrared observations to exert a strong influence on the forecast skill beyond 3–6 h indicates that their primary benefit may be improving short-range forecasts, though more extensive studies over longer time periods and different seasons are necessary to fully explore the impact of these observations on model forecast skill. These results are similar to those obtained during other assimilation studies employing cloud-sensitive observations, such as those from the Weather Surveillance Radar-1988 Doppler (WSR-88D) network, which have their greatest influence on short-range forecasts (e.g., Tong and Xue 2005; Zhang et al. 2009).

Future work includes exploring the potential synergy between high-resolution infrared brightness temperatures and WSR-88D radar reflectivity and radial velocity observations for improving the cloud structure in regional models. Regional-scale OSSEs will also be used to examine the ability of the three water vapor bands on the ABI sensor to exert a positive influence on high-impact precipitation and severe weather forecasts through a more accurate depiction of the 3D water vapor field. Last, a comprehensive effort to examine correlations between clear- and cloudy-sky infrared observations and the model state vector variables is also needed.

REFERENCES

Anderson, J. L., 2001: An ensemble adjustment Kalman filter for data assimilation. *Mon. Wea. Rev.,* **129,** 2884–2903.

——, 2007a: An adaptive covariance inflation error correction algorithm for ensemble filters. *Tellus,* **59A,** 210–224.

——, 2007b: Exploring the need for localization in ensemble data assimilation using a hierarchical ensemble filter. *Physica D,* **230,** 99–111.

——, 2009: Spatially and temporally varying adaptive covariance inflation for ensemble filters. *Tellus,* **61A,** 72–83.

——, T. Hoar, K. Raeder, H. Liu, N. Collins, R. Torn, and A. Avellano, 2009: The Data Assimilation Research Testbed: A community facility. *Bull. Amer. Meteor. Soc.,* **90,** 1283–1296.

Andersson, E., A. Hollingsworth, G. Kelly, P. Lonnberg, J. Pailleaux, and Z. Zhang, 1991: Global observing system experiments on operational statistical retrievals of satellite sounding data. *Mon. Wea. Rev.,* **119,** 1851–1864.

Baum, B. A., P. Yang, A. J. Heymsfield, S. Platnick, M. D. King, Y.-X. Hu, and S. T. Bedka, 2005: Bulk scattering properties for the remote sensing of ice clouds. Part II: Narrowband models. *J. Appl. Meteor.,* **44,** 1896–1911.

Bishop, C. H., and D. Hodyss, 2009a: Ensemble covariances adaptively localized with ECO-RAP. Part 1: Tests on simple error models. *Tellus,* **61A,** 84–96.

——, and ——, 2009b: Ensemble covariances adaptively localized with ECO-RAP. Part 2: A strategy for the atmosphere. *Tellus,* **61A,** 97–111.

Bouttier, F., and G. Kelly, 2001: Observing-system experiments in the ECMWF 4D-Var data assimilation system. *Quart. J. Roy. Meteor. Soc.,* **127,** 1469–1488.

Buehner, M., and M. Charron, 2007: Spectral and spatial localization of background-error correlations for data assimilation. *Quart. J. Roy. Meteor. Soc.,* **133,** 615–630.

Campbell, W. F., C. H. Bishop, and D. Hodyss, 2010: Vertical covariance localization for satellite radiances in ensemble Kalman Filters. *Mon. Wea. Rev.,* **138,** 282–290.

Chevallier, F., P. Lopez, A. M. Tompkins, M. Janiskova, and E. Moreau, 2004: The capability of 4D-Var systems to assimilate cloud-affected satellite infrared radiances. *Quart. J. Roy. Meteor. Soc.,* **130,** 917–932.

Collard, A. D., and A. P. McNally, 2009: The assimilation of Infrared Atmospheric Sounding Interferometer radiances at ECMWF. *Quart. J. Roy. Meteor. Soc.,* **135,** 1044–1058, doi:10.1002/qj.410.

Derber, J. C., and W.-S. Wu, 1998: The use of TOVS cloud-cleared radiances in the NCEP SSI analysis system. *Mon. Wea. Rev.,* **126,** 2287–2299.

Dudhia, J., 1989: Numerical study of convection observed during the Winter Monsoon Experiment using a mesoscale two-dimensional model. *J. Atmos. Sci.,* **46,** 3077–3107.

Evensen, G., 1994: Sequential data assimilation with a nonlinear quasi-geostrophic model using Monte Carlo methods to forecast error statistics. *J. Geophys. Res.,* **99** (C5), 10 143–10 162.

Gaspari, G., and S. E. Cohn, 1999: Construction of correlation functions in two and three dimensions. *Quart. J. Roy. Meteor. Soc.,* **125,** 723–757.

Hacker, J., J. L. Anderson, and M. Pagowski, 2007: Improved vertical covariance estimates for ensemble filter assimilation of near-surface observations. *Mon. Wea. Rev.,* **135,** 1021–1036.

Halem, M., E. Kalnay, W. E. Baker, and R. Atlas, 1982: An assessment of the FGGE satellite observing system during SOP-1. *Bull. Amer. Meteor. Soc.,* **63,** 407–429.

Hamill, T. M., J. S. Whitaker, and C. Snyder, 2001: Distance-dependent filtering of background error covariance estimates in an ensemble Kalman filter. *Mon. Wea. Rev.,* **129,** 2776–2790.

Han, Q., W. Rossow, R. Welch, A. White, and J. Chou, 1995: Validation of satellite retrievals of cloud microphysics and liquid water path using observations from FIRE. *J. Atmos. Sci.,* **52,** 4183–4195.

Heidinger, A. K., C. O'Dell, R. Bennartz, and T. Greenwald, 2006: The successive-order-of-interaction radiative transfer model. Part I: Model development. *J. Appl. Meteor. Climatol.,* **45,** 1388–1402.

Heymsfield, A. J., S. Matrosov, and B. Baum, 2003: Ice water path–optical depth relationships for cirrus and deep stratiform ice cloud layers. *J. Appl. Meteor.,* **42,** 1369–1390.

Hollingsworth, A., and P. Lönnberg, 1986: The statistical structure of short-range forecast errors as determined from radiosonde data. Part 1: The wind field. *Tellus,* **38A,** 111–136.

Hong, S.-Y., Y. Noh, and J. Dudhia, 2006: A new vertical diffusion package with an explicit treatment of entrainment processes. *Mon. Wea. Rev.,* **134,** 2318–2341.

Houtekamer, P. L., and H. L. Mitchell, 1998: Data assimilation using an ensemble Kalman filter technique. *Mon. Wea. Rev.,* **126,** 796–811.

——, and ——, 2001: A sequential ensemble Kalman filter for atmospheric data assimilation. *Mon. Wea. Rev.,* **129,** 123–137.

——, ——, G. Pellerin, M. Buehner, M. Charron, L. Spacek, and B. Hansen, 2005: Atmospheric data assimilation with an ensemble Kalman filter: Results with real observations. *Mon. Wea. Rev.,* **133,** 604–620.

Kain, J. S., and J. M. Fritsch, 1990: A one-dimensional entraining detraining plume model and its application in convective parameterization. *J. Atmos. Sci.,* **47,** 2784–2802.

——, and ——, 1993: Convective parameterization for mesoscale models: The Kain-Fritsch scheme. *The Representation of Cumulus Convection in Numerical Models, Meteor. Monogr.,* No. 24, Amer. Meteor. Soc., 165–170.

Kepert, J. D., 2009: Covariance localisation and balance in an Ensemble Kalman Filter. *Quart. J. Roy. Meteor. Soc.,* **135,** 1157–1176.

Le Marshall, J., and Coauthors, 2006: Improving global analysis and forecasting with AIRS. *Bull. Amer. Meteor. Soc.,* **87,** 891–894.

McCarty, W., G. Jedlovec, and T. L. Miller, 2009: Impact of the assimilation of Atmospheric Infrared Sounder radiance measurements on short-term weather forecasts. *J. Geophys. Res.,* **114,** D18122, doi:10.1029/2008JD011626.

McNally, A. P., 2009: The direct assimilation of cloud-affected satellite infrared radiances in the ECMWF 4D-Var. *Quart. J. Roy. Meteor. Soc.,* **135,** 1214–1229.

——, J. C. Derber, W. Wu, and B. B. Katz, 2000: The use of TOVS level-1b radiances in the NCEP SSI analysis system. *Quart. J. Roy. Meteor. Soc.,* **126,** 689–724, doi:10.1002/qj.49712656315.

——, P. D. Watts, J. A. Smith, R. Engelen, G. A. Kelly, J. N. Thepaut, and M. Matricardi, 2006: The assimilation of AIRS radiance data at ECMWF. *Quart. J. Roy. Meteor. Soc.,* **132,** 935–957.

Mitchell, H. L., P. L. Houtekamer, and G. Pellerin, 2002: Ensemble size, balance, and model-error representation in an ensemble Kalman filter. *Mon. Wea. Rev.,* **130,** 2791–2808.

Mlawer, E. J., S. J. Taubman, P. D. Brown, and M. J. Iacono, 1997: Radiative transfer for inhomogeneous atmospheres: RRTM, a validated correlated-k model for the longwave. *J. Geophys. Res.,* **102,** 16 663–16 682.

Mo, K. C., X. L. Wang, R. Kistler, M. Kanamitsu, and E. Kalnay, 1995: Impact of satellite data on the CDAS-reanalysis system. *Mon. Wea. Rev.,* **123,** 124–139.

Otkin, J. A., 2010: Clear and cloudy sky infrared brightness temperature assimilation using an ensemble Kalman filter. *J. Geophys. Res.,* **115,** D19207, doi:10.1029/2009JD013759.

——, and T. J. Greenwald, 2008: Comparison of WRF model-simulated and MODIS-derived cloud data. *Mon. Wea. Rev.,* **136,** 1957–1970.

——, ——, J. Sieglaff, and H.-L. Huang, 2009: Validation of a large-scale simulated brightness temperature dataset using SEVIRI satellite observations. *J. Appl. Meteor. Climatol.,* **48,** 1613–1626.

Polkinghorne, R., T. Vukicevic, and K. F. Evans, 2010: Validation of cloud-resolving model background data for cloud data assimilation. *Mon. Wea. Rev.,* **138,** 781–795.

Reale, O., J. Susskind, R. Rosenberg, E. Brin, E. Liu, L. P. Riishojgaard, J. Terry, and J. C. Jusem, 2008: Improving forecast skill by assimilation of quality-controlled AIRS temperature retrievals under partially cloudy conditions. *Geophys. Res. Lett.,* **35,** L08809, doi:10.1029/2007GL33002.

Schmit, T. J., M. M. Gunshor, W. P. Menzel, J. J. Gurka, J. Li, and A. S. Bachmeier, 2005: Introducing the next-generation Advanced Baseline Imager on GOES-R. *Bull. Amer. Meteor. Soc.,* **86,** 1079–1096.

Seaman, C. J., M. Sengupta, and T. H. Vonder Haar, 2010: Mesoscale satellite data assimilation: Impact of cloud-affected infrared observations on a cloud-free initial model state. *Tellus,* **62A,** 298–318.

Seeman, S. W., E. E. Borbas, R. O. Knuteson, G. R. Stephenson, and H.-L. Huang, 2008: Development of a global infrared land surface emissivity database for application to clear sky sounding retrievals from multispectral satellite radiance measurements. *J. Appl. Meteor. Climatol.,* **47,** 108–123.

Skamarock, W. C., J. B. Klemp, J. Dudhia, D. O. Gill, D. M. Barker, W. Wang, and J. G. Powers, 2005: A description of the Advanced Research WRF version 2. NCAR Tech. Note/TN-468+STR, 88 pp.

Stengel, M., M. Lindskog, P. Unden, N. Gustafsson, and R. Bennartz, 2010: An extended observation operator in HIRLAM 4D-VAR for the assimilation of cloud-affected satellite radiances. *Quart. J. Roy. Meteor. Soc.,* **136,** 1064–1074.

Thompson, G., P. R. Field, R. M. Rasmussen, and W. D. Hall, 2008: Explicit forecasts of winter precipitation using an improved bulk microphysics scheme. Part II: Implementation of a new snow parameterization. *Mon. Wea. Rev.,* **136,** 5095–5115.

Tong, M., and M. Xue, 2005: Ensemble Kalman filter assimilation of Doppler radar data with a compressible nonhydrostatic model: OSS experiments. *Mon. Wea. Rev.,* **133,** 1789–1807.

Torn, R. D., G. J. Hakim, and C. Snyder, 2006: Boundary conditions for limited-area ensemble Kalman filters. *Mon. Wea. Rev.,* **134,** 2490–2502.

Tracton, M. S., A. J. Desmarais, R. J. van Haaren, and R. D. McPherson, 1980: The impact of satellite soundings on the National Meteorological Center's analysis and forecast system—The Data Systems Test results. *Mon. Wea. Rev.,* **108,** 543–586.

Vukicevic, T., T. Greenwald, M. Zupanski, D. Zupanski, T. Vonder Haar, and A. Jones, 2004: Mesoscale cloud state estimation from visible and infrared satellite radiances. *Mon. Wea. Rev.,* **132,** 3066–3077.

——, M. Sengupta, A. S. Jones, and T. Vonder Haar, 2006: Cloud-resolving satellite data assimilation: Information content of IR window observations and uncertainties in estimation. *J. Atmos. Sci.,* **63,** 901–919.

Whitaker, J. S., and T. M. Hamill, 2002: Ensemble data assimilation without perturbed observations. *Mon. Wea. Rev.,* **130,** 1913–1924.

Xu, J., S. Rugg, L. Byerle, and Z. Liu, 2009: Weather forecasts by the WRF-ARW model with GSI data assimilation system in complex terrain areas of southwest Asia. *Wea. Forecasting,* **24,** 987–1008.

Yoon, Y.-N., E. Ott, and I. Szunyogh, 2010: On the propagation of information and the use of localization in ensemble Kalman filtering. *J. Atmos. Sci.,* **67,** 3823–3834.

Zhang, F., Y. Weng, J. A. Sippel, Z. Meng, and C. H. Bishop, 2009: Cloud-resolving hurricane initialization and prediction through assimilation of Doppler radar observations with an Ensemble Kalman Filter. *Mon. Wea. Rev.,* **137,** 2105–2125.